Deterministic three-dimensional self-assembly of Si through a rimless and topology-preserving dewetting regime

Meher Naffouti,[1,2,*] Marco Salvalaglio,[3,†] Thomas David,[1,*] Jean-Benoît Claude,[1,‡] Monica Bollani,[4] Axel Voigt,[3,5] Abdelmalek Benkouider,[1,*] Luc Favre,[1] Antoine Ronda,[1] Isabelle Berbezier,[1] Anne Delobbe,[6] Arnaud Houel,[6] and Marco Abbarchi[1,§]

[1]*Aix Marseille Université, Université de Toulon, CNRS, IM2NP, Marseille, France*

[2]*Laboratoire de Micro-Optoélectronique et Nanostructures, Faculté des Sciences de Monastir Université de Monastir, 5019 Monastir, Tunisia*

[3]*Institute of Scientific Computing, Technische Universität Dresden, 01062 Dresden, Germany*

[4]*Istituto di Fotonica e Nanotecnologie-Consiglio Nazionale delle Ricerche, Laboratory for Nanostructure Epitaxy and Spintronics on Silicon, Via Anzani 42, 22100 Como, Italy*

[5]*Dresden Center for Computational Materials Science, Technische Universität Dresden, 01062 Dresden, Germany*

[6]*Orsay Physics, 13710 Fuveau, France*

(Received 15 May 2019; revised manuscript received 11 August 2019; published 7 October 2019)

Capillary-driven mass transport in solids is typically understood in terms of surface-diffusion limited kinetics, leading to conventional solid-state dewetting of thin films. However, another mass transport mechanism, so-called surface-attachment/detachment limited kinetics, is possible. It can shrink a solid film, preserving its original topology without breaking it in isolated islands, and leads to faster dynamics for smaller film curvature in contrast with the opposite behavior observed for surface-diffusion limited kinetics. In this work, we present a rimless dewetting regime for Si, which is ascribed to effective attachment-limited kinetics mediated by the coexistence of crystalline and amorphous Si phases. Phase-field numerical simulations quantitatively reproduce the experimental observations, assessing the main mass transport mechanism at play. The process can be exploited to obtain in a deterministic fashion monocrystalline islands (with 95% probability) pinned at ≈500 nm from a hole milled within closed patches.

DOI: 10.1103/PhysRevMaterials.3.103402

I. INTRODUCTION

Thin films of organic or inorganic compounds have the tendency to break as a consequence of the minimization of their surface energy density. When perturbed, liquid [1], polymer [2], and crystalline films [3] bead over time by dripping into tiny droplets featuring a particular size and shape determined by the interactions with the substrate, the surrounding atmosphere, and the initial film thickness.

Although dewetting of metals is a phenomenon conveniently exploited for important applications [4] (such as the formation of gold seeds for vapor-liquid-solid growth of nanowires [5]), its use in silicon is largely unexplored in spite of the manifold advantages it offers with respect to common bottom-up and top-down nanofabrication methods. Being a spontaneous phenomenon driving significant and controllable changes of morphologies, it offers interesting technological perspectives. Indeed, it has been exploited to (i) implement a three-dimensional (3D) Si island in a strain-free system (in contrast with the conventional Stranski-Krastanov approach used in IV-IV and III-V semiconductor compounds) [6]; (ii) form monocrystalline and faceted (atomically smooth) structures, free from defects and from the typical roughness produced by conventional etching methods [7–10]; (iii) directly fabricate monocrystalline islands on electrically insulating substrates (SiO_2) [11]; (iv) frame, when assisted by templates, complex, monocrystalline and ordered nanoarchitectures, with the additional advantage of reduced etching time with respect to conventional lithographic approaches [12,13]; (v) form dielectric metasurfaces for application in photonics at visible and near-infrared frequencies [9,14–16]; (vi) implement devices over large scales in a time that is independent of their size; (vii) tune the size of the particles by setting the initial film thickness and independently tune their density by adding germanium during growth [16]; and (viii) obtain core-shell structures [10].

So far, shape instabilities of thin crystalline films have been attributed mainly to capillary-driven mass transport at the crystal surface [17,18] and are well understood in terms of *surface diffusion limited kinetics* (SD) [19–25]. In this regime, common to metals and semiconductors, the film retracts forming a thick rim. In turn, the rim undergoes further instabilities (such as bulging and finger formation) and finally breaks into isolated islands. In templated crystalline films of semiconductors and metals, a remarkable example of dewetting via SD is the spontaneous pattern formation of complex nanoarchitectures [13,26–28].

*Present address: X-FAB France SAS 224, Boulevard John Kennedy, 91105 Corbeil-Essonnes Cedex, France.

†Corresponding author; marco.salvalaglio@tu-dresden.de

‡Present address: Aix-Marseille Université, CNRS, Centrale Marseille, Institut Fresnel, Marseille, France.

§Corresponding author; marco.abbarchi@im2np.fr

 ©2019 American Physical Society

A different capillary-driven shape evolution ruled by *surface attachment limited kinetics* (SALK) was proposed in 1995 by Cahn and Taylor [29] and thoroughly discussed by Carter and coworkers [30] for faceted crystals [31]. Such dynamics occurs when the phase surrounding the solid (e.g., a fluid, such as the atmosphere, or a thin surface layer having different properties) allows fast transport of atoms. In this case, the attachment or detachment of atoms to the surface of the solid is the rate-limiting step [30,32,33]. If the surrounding fluid is the fast transport pathway, the mechanism is known as evaporation-condensation.

This mechanism has not yet been reported in the context of single-crystal thin-film dewetting. However, SALK at play in these systems would lead to a peculiar dynamics including volume conservation and shape-preserving evolution: In contrast with SD, no isolated islands are expected at the end of the process and one individual object preserves its topology while shrinking, as illustrated in Ref. [30]. Thus, given the broad interest in the stability of thin films, providing the conditions to realize and control this unexplored self-assembly method is of the utmost importance.

Here we report on solid-state dewetting of ultrathin, monocrystalline, solid films of silicon on SiO_2 (UT-SOI) which may be ascribed to SALK. A partially amorphous layer atop of a UT-SOI is obtained by patterning trenches and closed patches via focused ion beam. This amorphous layer provides the high-mobility phase necessary for fast mass transport during annealing while recrystallization takes place. Early stages of dewetting show the absence of a receding rim, a uniform thickening of the Si layer, and a faster dewetting speed for larger patches with a corresponding lower height. This evidence is benchmarked against phase-field simulations of stripes and closed patches evolving under SALK. Finally, we show that this process can be controlled by milling pierced patches for the deterministic fabrication (with ≈95% probability over 180 trials) and positioning (within ≈500 nm from the milled hole) of monocrystalline silicon islands. The island size is, to a first approximation, independent on the initial patch surface.

II. RESULTS

A. Experimental methods

An 11-nm-thick UT-SOI on a 145-nm-thick buried oxide was milled with free patterns (e.g., trenches, circles, squares, pits) with a liquid-metal ion-source focused ion beam (FIB, Ga^+ ions, milling current about 10 pA, beam energy 30 keV) and annealed at 780 °C in ultrahigh vacuum (Fig. 1, further details of the experimental methods are reported in the Supplementary Material [SM] [34]) [9,12,15]. Two monolayers of Ge were supplied to enhance the surface diffusion and trigger the dewetting. From electron diffraction spectroscopy after dewetting, we estimate a Ge content of 2%, which is close to the sensitivity of the instrument (not shown).

B. Experimental results

We first compare the evolution of square patches etched via FIB against the case of electron beam lithography and reactive ion etching (e-beam and RIE, Fig. 2). Details for this

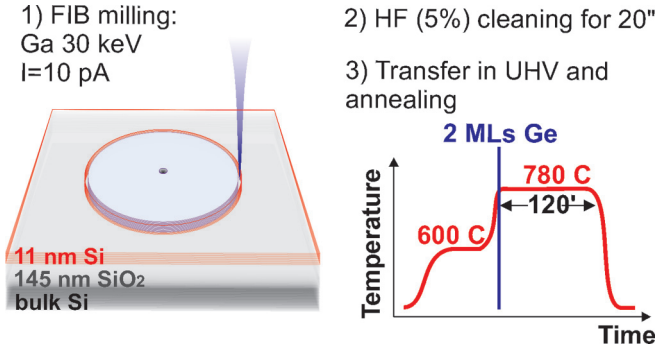

FIG. 1. (1) Scheme of the UT-SOI (initial thickness h_0 = 11-nm-thick UT-SOI atop 145-nm-thick buried oxide, BOX) and liquid-metal ion-source focused ion beam used to mill free patterns (e.g., trenches, squares, circles, pits, etc); (2) removal of native oxide via wet etching; (3) annealing in the ultrahigh vacuum (UHV) of a molecular beam epitaxy reactor. First, the samples are annealed at 600 °C for 30 min followed by deposition of two monolayers of Ge and finally annealed at 780 °C for 120 min.

second case are provided in Refs. [13,28]. AFM profiles at the edge of the patches [Fig. 2(c)] show a partial dewetting of the UT-SOI for both cases and a lacking rim for the FIB case in stark contrast with the e-beam and RIE case. Furthermore, in addition to the ≈30-nm-thick rim all along the perimeter of the patch found for the e-beam and RIE case, protrusions are formed at its corners as also predicted by sharp interface models [35–38]. These protrusions eventually lead to four islands depending on the initial aspect ratio of the square patch [13]. None of these features is observed when etching via FIB.

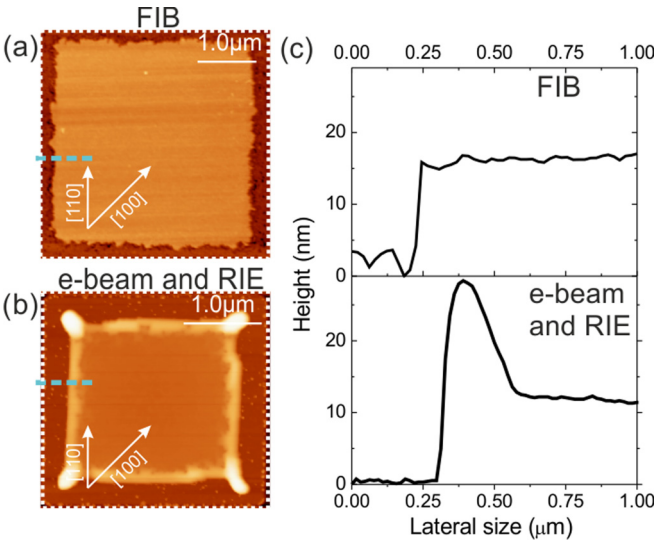

FIG. 2. (a) Square patch etched via FIB after annealing. The white dashed square highlights the original shape of the patch before annealing. (b) Square patch etched via e-beam lithography and reactive ion etching (e-beam and RIE) after annealing (see Ref. [13] for details). The white dashed square highlights the original shape of the patch before annealing. (c) Comparison between the patch edge profile after annealing for both FIB (top panel) and e-beam and RIE (bottom panel) etching extracted from panels (a) and (b) (highlighted by dashed lines).

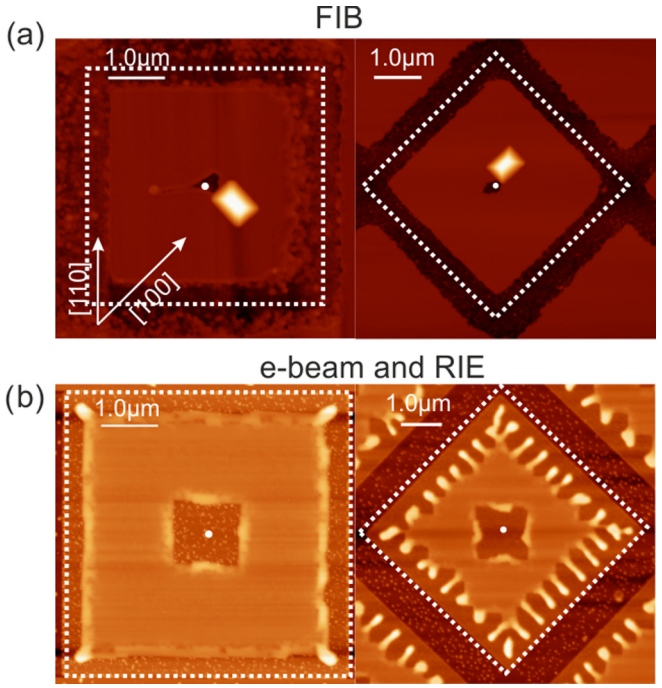

FIG. 3. (a) Left (right) panel: square patch etched via FIB after annealing oriented along the [110] ([100]) crystallographic direction. The white dashed square highlights the original shape of the patch before annealing. In both cases, a submicrometric, rectangular island is formed next to the central hole after annealing. (b) Left (right) panel: square patch etched via e-beam lithography and reactive ion etching oriented along the [110] ([100]) crystallographic direction after annealing. The white dashed square highlights the original shape of the patch before annealing. See Ref. [13] for more details on this case.

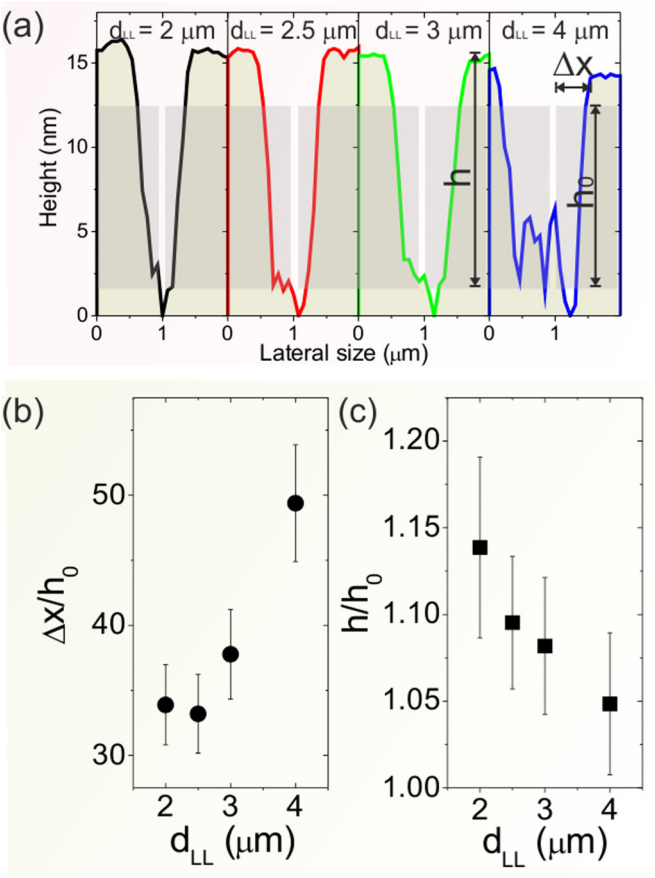

FIG. 4. (a) Height profile obtained from AFM images of parallel trenches etched by FIB after dewetting. An example of the AFM image showing the full patch width is provided in the SM [34]. From the left to the right panels, $d_{LL} = 2$, 2.5, 3, and 4 μm. Shaded areas highlight the original shape of the UT-SOI before annealing. h_0 highlights the original film height and h is its final height. Δx is a measure of the edge retraction distance from its original position before dewetting. (b) Retraction distance Δx (in unity of h_0) as a function of d_{LL}. (c) Film height h (in unity of h_0) as a function of d_{LL}. h, x, and the experimental errors are determined as average values and standard deviations over ten measurements. See also the SM [34].

Further insight in the peculiarities of FIB etching with respect to e-beam and RIE can be obtained by modifying the initial patch design (Fig. 3) by milling a small hole at their center. When using FIB milling, we observe the formation of an island in contrast to the e-beam and RIE case where a complex behavior takes place with formation of rims and protrusion also around the central hole [13]. Moreover, by comparing the evolution of patches oriented along the stable dewetting front ([110] in-plane crystallographic direction) with the unstable counterpart ([100]), we observe an identical outcome for the FIB milling (no rim and a single island at the center of the patch) against a completely different outcome in the e-beam and RIE case (bulging and fingers formation along the unstable dewetting front). Note that this latter feature is commonly observed for SD dewetting of thin silicon films [6,22,24,39–42].

A more systematic analysis of dewetting after FIB milling is provided for patches having different lateral width obtained from parallel trenches etched with different spacing [line-to-line distance d_{LL}, Fig. 4(a)]. An example of a patch obtained from parallel trenches is shown in the SM, whereas here we focus only on their edges. Edge retraction (Δx) and patch height (h) are measured in 10 distinct points. The corresponding values and error bars are obtained as average and standard deviation for each d_{LL}. This analysis highlights a faster dewetting speed for larger patches and a corresponding slightly lower film height [Figs. 4(b) and 4(c)]. This feature is in contrast with the conventional case of SD, where larger curvatures (smaller patch width) lead to faster kinetics. Height fluctuations, reflected by the error bars, are in the range of about 1 nm (one order of magnitude lower than the rim thickness found in SD dewetting).

In order to understand the origin of these differences between the two dewetting dynamics, we perform microscopic analysis of the initial state of the Si crystal after FIB etching. Apart from sputtering, ion milling has several consequences on the adjacent areas (Fig. 5). A monocrystalline (001) Si sample etched via FIB in parallel trenches shows implantation of the Ga^+ ions used for milling and consequent amorphization of the superficial layers [below the etched trenches up to ≈70 nm deep, dark area am-Si in Figs. 5(a) and 5(b)] as well as in the nearby areas. More precisely, at ≈800 nm from the milled trenches the silicon is crystalline (cr-Si), at

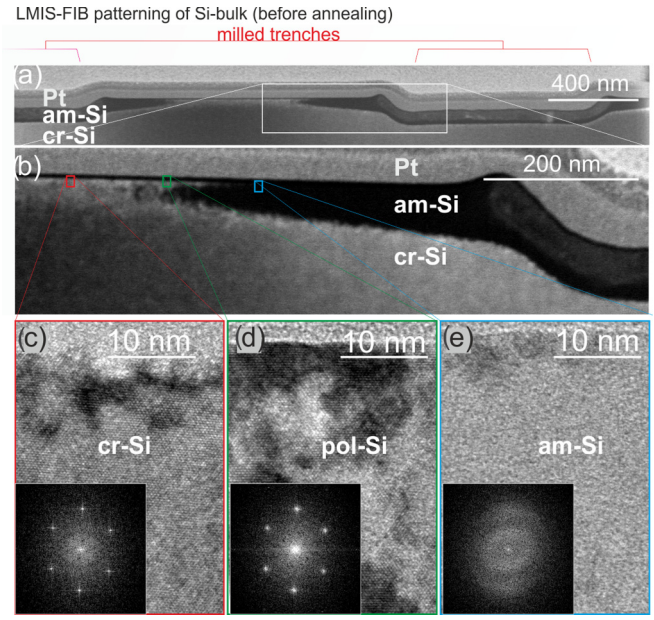

FIG. 5. (a) Dark-field TEM image of Si bulk (001) milled with a Ga^+ FIB. The platinum (Pt) protecting the TEM lamella, the amorphous (am-Si) and crystalline (cr-Si) silicon are highlighted. (b) An enlargement of the area highlighted in panel (a). [(c)–(e)] Enlargements of the rectangles shown in panel (b). For each case, the two-dimensional (2D) Fourier transform is shown.

≈700 nm the crystal shows some disorder (pol-Si), whereas at ≈600 nm the material is amorphous (am-Si). A similar analysis on thin films on insulators shows that the FIB-induced amorphization of the top layers extends over micrometer distances (further details are shown in SM [34]), confirming previous reports [43] and pointing out that patches having an extension of a few μm have their superficial layers partially amorphized.

Unlike in FIB milling, this amorphous layer is not present in crystalline materials etched by RIE. In fact, in this latter case, the surface of the patches is protected by a resist or a metallic mask and only the exposed parts are affect by the etching, eventually leading to some roughness on the sidewalls in the range of ≈10 nm [44]. Thus, the dewetting dynamics of UT-SOI patches etched by e-beam and RIE can be simply ascribed to SD [13,17,18,35–38].

The evolution observed in patches etched by FIB shows compelling similarities with the features typical of SALK, which is enabled by the presence of a high-mobility phase at the surface [30]. Owing to the much larger atom mobility of amorphous silicon with respect to the crystalline counterpart (with a difference of two orders of magnitude in the diffusion coefficient [45]), a reservoir of mobile material is present at the patch edges (as well as at its surface). This leads to an effective fast material redistribution over long distances (not limited by the film curvature as in SD) from the edges to the center.

In the following section, the comparison of the experimental data with simulations reproducing the SALK dynamics is shown, assessing the main features of the mechanism at play during the evolution.

III. PHASE FIELD SIMULATIONS AND COMPARISON WITH EXPERIMENTS

The outward-normal velocity of a surface evolving by SALK is $v_{\mathrm{SALK}} = M(K - \mu)$, with M being a mobility coefficient depending on the material properties (such as the density of attachment sites and the attachment rate [30]), μ being the local chemical potential on the surface, and K being the average of the chemical potential along the surface to impose volume conservation. For isotropic surface energies, μ is proportional to the local surface curvature κ. This dynamics ruled by SALK and described by v_{SALK} differs from that by SD, as $v_{\mathrm{SD}} \propto \nabla_\Gamma^2 \mu$ with ∇_Γ^2 the Laplacian evaluated along the surface (Γ). Material transport under SALK prevents the local accumulation of mass typical of SD leading to nonconventional dewetting features, such as a bulk thickening of the film, shape preservation, and lack of a receding rim [30].

To assess the analogies of the morphological evolution reported above with SALK, phase-field numerical simulations were performed [46,47]. This approach can deal with complex evolution possibly including topological changes regardless of the dimensionality of the system: an auxiliary order parameter, φ (set to 1 in the solid and 0 on the outside with a continuous variation in between), is considered to define implicitly the surface of the solid phase as the isosurface $\varphi = 0.5$. Morphological evolution of the solid is obtained by setting the evolution law for φ [47,48], here meant to reproduce v_{SALK}. Within the considered phase field approach, SALK is accounted for by

$$\frac{\partial \varphi}{\partial t} = \epsilon \Delta \varphi + \frac{1}{\epsilon}[B'(\varphi) + \alpha], \tag{1}$$

with $B(\varphi) = 18\varphi^2(1-\varphi)^2$ and ϵ being a parameter controlling the extension of the interface between phases. α is a term enforcing mass conservation at each time [46,49,50]:

$$\alpha = \frac{\sqrt{2B(\varphi)}}{\int_\Omega \sqrt{2B(\varphi)} d\Omega} \int_\Omega B'(\varphi) d\Omega, \tag{2}$$

with Ω being the simulation domain. No-flux boundary conditions are considered, enforcing a contact angle of 90° with respect to the substrate. We consider isotropic surface-energy focusing on the features of the process neglecting the additional contributions of surface faceting (although feasible within the phase-field framework [51–54]). Moreover, the same framework can be adapted to account in detail for other mechanisms occurring at the surface and driving forces (see, e.g., Refs. [55,56]). The simulations were performed exploiting the finite-element toolbox AMDiS [57,58] and established numerical methods for phase-field approaches [59]. Additional details about the model are reported in the SM [34].

We first compare full-3D simulations of square patches having an aspect ratio of 1/40 evolving under SALK and SD (Fig. 6). In the first case, we observe a rimless, conformal dewetting with a homogeneous thickening of the patch, whereas in the second case rim and protrusion at the corners are found, as expected for pure SD dewetting dynamics [26,27,35–38]. For more details on simulations of SD, see Ref. [13]). This 3D case is of particular interest as differences with respect to standard SD dewetting leading to rims and protrusion at the patch corners are very evident and are

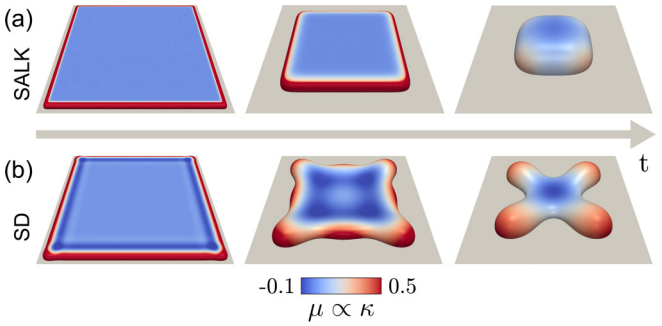

FIG. 6. (a) 3D phase-field simulations reproducing the dewetting by SALK of a patch having aspect ratio 1/40. (b) Same as in panel (a) for SD dynamics (for more details on this case, see Ref. [13]).

similar to those previously discussed for the experimental cases (Fig. 2).

Owing to the high-temperature annealing used to induce the dewetting, the amorphous phase is not only partially displaced toward the center of the patches but it is also recrystallized. This second process is confirmed by transmission electron microscopy (TEM) imaging after annealing showing a slight crystal disorder in the area affected by the FIB amorphization (see the SM [34]). This implies that the SALK regime can be only observed in a relatively short time window, rendering a comparison of the 3D temporal dynamics of square patches with simulations (e.g., as those shown in Ref. [13]) not feasible.

A quantitative comparison between data and theory is provided for the evolution of long patches having different lateral width d_{LL}. The 2D phase-field simulations of dewetting via SALK were performed to compare with film aspect ratios $r_1 = 1/200$ and $r_2 = 1/400$, mimicking $d_{LL} = 2$ μm and $d_{LL} = 4$ μm (Fig. 4). A rimless thickening of the film is observed, together with a faster dewetting for larger stripes [Figs. 7(a) and 7(b) and Supplemental Material [34]). In fact, these trenches are further away from the equilibrium with respect to more closely spaced ones: the lower values of K for large stripes lead to larger driving forces at the edges of the film where $\mu > K$, against a smaller tendency to thickening at its center as $\mu \sim 0$ and $v_{SALK} \sim K$.

Deeper insight can be obtained from Figs. 7(b) and 7(c), where a faster dewetting speed for r_2 against a faster thickening for r_1 is shown during the evolution toward equilibrium. This is in qualitative agreement with the experiments [Figs. 4(b) and 4(c)]. Finally, a direct comparison between theory and experiments for all the four investigated patch width shows a good agreement for time step $t = 4$, supporting the SALK-like dewetting mechanism at play [Fig. 7(d)].

We conclude this section observing that dewetting via SALK is mass preserving. This is accounted for by a precise evaluation of the mass displacement from the sides of the patches toward their center (and eventually feeding the central island in pierced patches) as shown in the SM [34].

IV. SELF-ASSEMBLY OF ISLANDS

Islands formation is often observed in closed patches especially when a central pit is milled at their center [Fig. 3(a)].

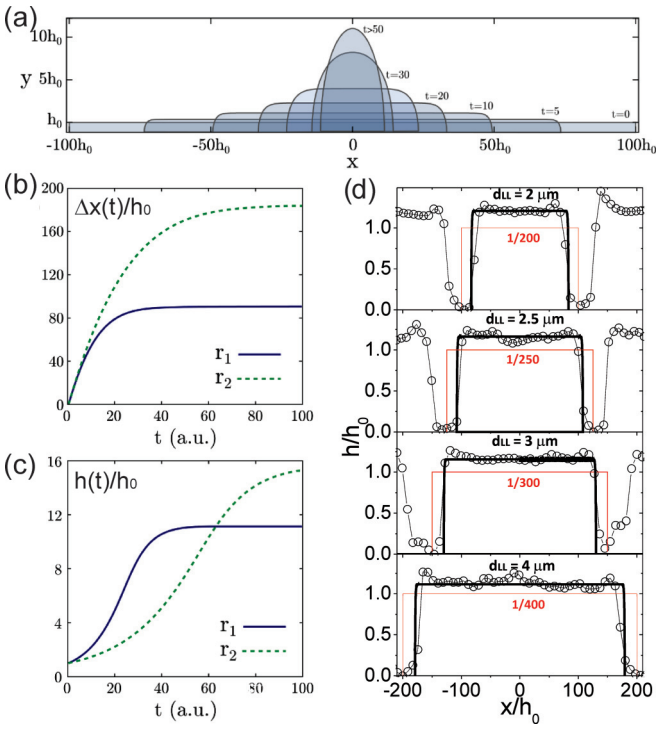

FIG. 7. (a) Representative stages of the evolution by SALK of a rectangle (the cross section of a stripe) with height-to-base aspect ratio $r_1 = 1/200$. Time is expressed in arbitrary units. Simulation are performed with $h_0 = 1$. (b) Edge displacement over time for patches with $r_1 = 1/200$ and $r_2 = 1/400$. (c) Thickening over time for profiles with r_1 and r_2 (see also video in Ref. [34]). (d) Comparison between experimental and theoretical profiles. The red curve represents the initial condition of the UT-SOI before annealing, the black line represents the film at $t = 4$, and the symbols are the experimental data (see also the SM [34]).

Thus, we considered different patch sizes, shapes (triangle, circle, square), presence or lack of a central pit, and orientations with respect to the crystallographic axes, in order to study and drive this phenomenon.

The general picture is described as follows:

(1) For small patches (aspect ratio >1/230), the film is shrunk and a pyramidal island is found at the edge [Fig. 8(a), left panel].

(2) For larger patches, the film is shrunk but no island is observed [Fig. 8(a), central panel].

(3) For pierced patches, the film is shrunk and the formation of the island is triggered next to the hole [Fig. 8(a), right panel].

These features are common to all the investigated patch shapes (e.g., square, circle, or triangle), sizes, and orientations with respect to the crystallographic axes.

The presence of an island depends on the patch size and the presence of holes in a highly reproducible fashion, as shown by the probability of forming a single island within a patch [$p(1)$] as a function of the initial patch surface $S_0 = L^2$ [Fig. 8(b)]. Without a hole and $S_0 > 10$ μm^2, $p(1)$ is below 0.5 and it shows a decreasing trend when increasing S_0; for smaller S_0, $p(1)$ approaches 1 and the islands are found at the patch edges. For pierced patches, $p(1)$ is always larger than 0.8 and it approaches 1 for $S_0 < 10$ μm^2.

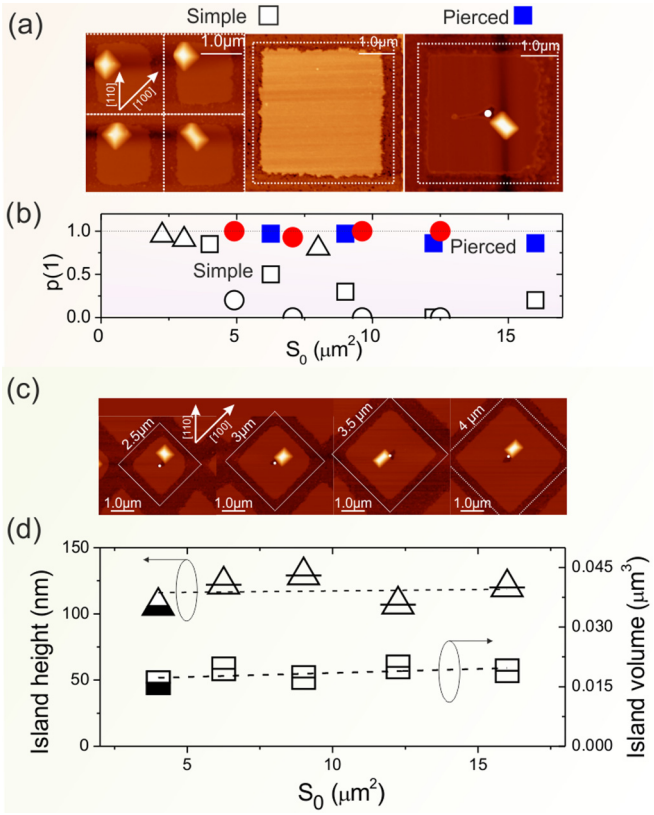

FIG. 8. (a) Respectively from the left to the right panels: four replicas of $L = 2$ μm squares, $L = 4$ μm square, and a pierced $L = 4$ μm square. The white lines highlight the FIB milling. The white dashed lines highlight the etched trenches and pit. (b) Island formation probability $p(1)$. Full symbols: probability $p(1)$ to form one and only one island pinned by the central hole in pierced patches, as a function of $S_0 = L^2$. Empty symbols: $p(1)$ (regardless of its position within the patch) as a function of S_0 for simple (nonpierced) shapes. The symbol shape corresponds to the patch shape. Each point represents at least 20 repetitions of the same patch size and shape. The statistics merge patches oriented along the [110] and [100] directions. (c) From the left to the right panel: pierced, squared patches oriented along the [100] crystallographic direction. The patch side L ranges between 2.5 and 4 μm. The white dashed lines highlight the etched trenches and pit. (d) Island volume (right axis) and height (left axis) extracted from (c) as a function of the initial patch surface. Lines are linear fit to the data. The first points ($S_0 = 4$ μm^2) are relative to a nonpierced squared patch [as those shown in panel (a), left panel].

A remarkable peculiarity of the islands formed via SALK with respect to those obtained via conventional SD is that in the former case all the islands have a similar size irrespective of the starting patch extension [Figs. 8(c) and 8(d)], whereas in the latter case the initial patch surface and UT-SOI thickness set the final island dimension [12,15]. This suggests that size tuning by simply controlling the dewetting time could be achieved.

V. DISCUSSION

Although rimless dewetting has been reported earlier in thin films of metals (e.g., Ag [60], Fe [61], and Al [62]), in all these cases the material was polycrystalline. As such, these examples should not be confused with our report, where the underlying material is monocrystalline UT-SOI surrounded by a high-mobility, amorphous phase. A rimless morphology, *per se*, does not account for SALK-like dewetting and it is not inconsistent with the diffusion-controlled process. In fact, it was attributed to SD combined with diffusion along the grain boundaries [60,61] and along the film-substrate–over-layer interfaces [61,62]. The features of SALK-based dewetting go beyond this specific aspect common to other systems as it also involves (1) a faster retraction speed for lower overall curvature and (2) a bulk thickening of the solid that was not reported in the aforementioned cases. Similar considerations hold for the case of UT-SOI dewetting [63,64] for patterned patches and spontaneous dewetting [45]: These rimless processes did not account for SALK but were interpreted as conventional SD dewetting. Besides, the partial characterization of the system does not allow for a more direct comparison.

The ordering of Si islands is a necessary step for any attempt to integrate these structures into existing Si-based electronic devices (owing to the need for mandatory spatial addressability). In our case, the underlying SALK-like process at play allows forming Si islands directly on pristine UT-SOI, a possibility forbidden in homoepitaxy as well as in conventional solid-state dewetting evolving under SD, where the buried oxide is completely denuded. Conventional hybrid top-down–bottom-up methods for deterministic 3D islands formation rely on complex fabrication steps (e.g., e-beam lithography and reactive ion etching) and epitaxial growth employing strain [65] (Stransky-Krastanov). In contrast, our method is a direct FIB milling process followed by annealing.

The size homogeneity of the dewetted islands, irrespective of the initial patch extension, is also a fingerprint of the main role played by amorphization of the UT-SOI skin. This is in stark contrast with conventional dewetting via SD and in general with most self-assembly processes (e.g., nucleation via Stranski-Krastanov). This feature is important in view of the formation of 3D nano-objects on thicker SOI and could potentially permit the fabrication of AFM tips and cantilevers [66]. The range of applicability of our method for Si islands goes beyond that: Dielectric Mie resonators [9,14,15], solid-state memories, and strain arrays for 2D materials [67] are only a few examples of possible uses. Furthermore, given the similarities commonly found between dewetting of thin films of metals and semiconductors, we expect that, in analogy with the SD regime [13,27,28], such SALK-like process can be extended to metals, which will further widen the range of applicability of our method.

By comparing our results with similar samples etched by FIB and annealed at a higher temperature (quickly recrystallized, see the SM [34]), we confirm that the SALK-like features are specific of the amorphous phase surrounding the crystalline patch. In pierced and quickly re-crystallized solids [12], we observe the features of SD: Formation of islands occurs at the patch corners or edges whereas no island is observed near the central hole.

Unlike what is expected for an anisotropic mass transport on a crystal evolving under SD (different dewetting speed along stable and unstable dewetting fronts, Fig. 3(b) [68,69]), we observe the same dewetting outcomes for patches

oriented along [110] and [100] axes (Fig. 3), further supporting the hypothesis of mass transport through the amorphous phase.

Despite the high reproducibility of the experimental results (tested also in other samples), justifying the island formation from analytical or numerical modeling is not straightforward: Nucleation events for the island (that cannot be traced back to energy considerations leading to SALK or SD) should be taken into account. Moreover, a full model including the recrystallization dynamics in 3D (and not only an effective model focusing on the material transport at the surface) should be considered to capture the different morphologies and it is far beyond the scope of the present work. Nonetheless, we observe that all the rectangular islands have sides oriented along the [100] and [010] in-plane crystallographic directions. This is a feature often observed in (Si)Ge-based structures on Si-based (001)-oriented substrates, nucleated via the Stranski-Krastanov mechanism [70–72]. This analogy suggests that local strain accumulation nearby the central pit during dewetting may be the origin of island formation in our system.

Based on the results obtained for trenches, the central hole in pierced patches can be regarded as a dewetting front expelling mass but, at the same time, competing with the fast fluxes coming from the edges. Owing to the reduction of the dewetting speed at the center of the patch and to the local thickening of the layer fed by the inward flux from the edges, mass can be accumulated. Other local conditions (e.g., strain accumulation, facet formation during recrystallization) may act as seeds for island formation.

VI. CONCLUSIONS

In conclusion, we realized the experimental conditions achieving a peculiar dewetting regime whose main feature corresponds to surface attachment limited kinetics. In contrast to conventional surface diffusion, the dewetting kinetics is here faster for lower average curvatures, occurs without rim formation, and brings a solid film to thicken while shrinking, as accounted for by experiments, numerical simulations, and their detailed comparison. As a result, the breakup of the thin film, typical of standard dewetting mechanisms, is prevented. Beyond fundamental interest in this mass transport process for Si thin films, we also demonstrated that it can be efficiently exploited to deterministically form monocrystalline sub-micrometric islands sitting on large patches of pristine UT-SOI. Our approach provides an alternative way to form 3D islands and combines the benefits of top-down fabrication and bottom-up self-assembly (e.g., atomically smooth islands). Beyond the experimental evidence of this mass transport regime in a dewetting process for Si, this method is a distinct approach for specific applications such as the implementation of position-controlled, nanocrystal-based memory devices, dielectric Mie resonators, and cantilever tips for atomic force microscopes.

ACKNOWLEDGMENTS

We acknowledge the projects PHC MAGHREB (No. 32595SL), EMMAG-Erasmus Mundus Maghreb and Egypt, the EU H2020 R&I programme (No. 654148 LASERLAB Europe-ARES), the PRCI-ULYSSES (No. ANR-15-CE24-0027-01), and the FET-OPEN project NARCISO (No. 828890). M.S. acknowledges the support of the Alexander von Humboldt Foundation. We also gratefully acknowledge the computing time granted by the John von Neumann Institute for Computing (NIC) and provided on the supercomputer JURECA at Jülich Supercomputing Centre (JSC), within Project No. HDR06, and by the Information Services and High Performance Computing (ZIH) at TU Dresden. We thank the Nanotecmat Platform of the IM2NP Institute of Marseille. The authors thank Dominique Chatain and Rachel Zucker for useful discussions.

[1] B. Derby, Annu. Rev. Mater. Res. **40**, 395 (2010).
[2] G. Reiter, Phys. Rev. Lett. **68**, 75 (1992).
[3] C. V. Thompson, Annu. Rev. Mater. Res. **42**, 399 (2012).
[4] D. Gentili, G. Foschi, F. Valle, M. Cavallini, and F. Biscarini, Chem. Soc. Rev. **41**, 4430 (2012).
[5] H. J. Fan, P. Werner, and M. Zacharias, Small **2**, 700 (2006).
[6] F. Leroy, Ł. Borowik, F. Cheynis, Y. Almadori, S. Curiotto, M. Trautmann, J. C. Barbé, and P. Müller, Surf. Sci. Rep. **71**, 391 (2016).
[7] E. Sutter and P. Sutter, Nanotechnology **17**, 3724 (2006).
[8] M. Aouassa, I. Berbezier, L. Favre, A. Ronda, M. Bollani, R. Sordan, A. Delobbe, and P. Sudraud, Appl. Phys. Lett. **101**, 013117 (2012).
[9] M. Abbarchi, M. Naffouti, B. Vial, A. Benkouider, L. Lermusiaux, L. Favre, A. Ronda, S. Bidault, I. Berbezier, and N. Bonod, ACS Nano **8**, 11181 (2014).
[10] M. Naffouti, T. David, A. Benkouider, L. Favre, M. Cabie, A. Ronda, I. Berbezier, and M. Abbarchi, Nanotechnology **27**, 305602 (2016).
[11] P. Sutter, W. Ernst, Y. Choi, and E. Sutter, Appl. Phys. Lett. **88**, 141924 (2006).
[12] M. Naffouti, T. David, A. Benkouider, L. Favre, A. Delobbe, A. Ronda, I. Berbezier, and M. Abbarchi, Small **12**, 6115 (2016).
[13] M. Naffouti, R. Backofen, M. Salvalaglio, T. Bottein, M. Lodari, A. Voigt, T. David, A. Benkouider, I. Fraj, L. Favre *et al.*, Sci. Adv. **3**, eaao1472 (2017).
[14] M. Naffouti, T. David, A. Benkouider, L. Favre, A. Ronda, I. Berbezier, S. Bidault, N. Bonod, and M. Abbarchi, Nanoscale **8**, 7768 (2016).
[15] T. Wood, M. Naffouti, J. Berthelot, T. David, J.-B. Claude, L. Métayer, A. Delobbe, L. Favre, A. Ronda, I. Berbezier *et al.*, ACS Photonics **4**, 873 (2017).
[16] M. Bouabdellaoui, S. Checcucci, T. Wood, M. Naffouti, R. P. Sena, K. Liu, C. M. Ruiz, D. Duche, J. le Rouzo, L. Escoubas *et al.*, Phys. Rev. Mater. **2**, 035203 (2018).
[17] D. Srolovitz and S. Safran, J. Appl. Phys. **60**, 247 (1986).
[18] D. Srolovitz and S. Safran, J. Appl. Phys. **60**, 255 (1986).
[19] D. T. Danielson, D. K. Sparacin, J. Michel, and L. C. Kimerling, J. Appl. Phys. **100**, 083507 (2006).
[20] Y. Fan, R. Nuryadi, Z. A. Burhanudin, and M. Tabe, Japanese J. Appl. Phys. **47**, 1461 (2008).
[21] C. M. Muller and R. Spolenak, Acta Mater. **58**, 6035 (2010).

[22] M. Dufay and O. Pierre-Louis, Phys. Rev. Lett. **106**, 105506 (2011).

[23] F. Cheynis, E. Bussmann, F. Leroy, T. Passanante, and P. Müller, Phys. Rev. B **84**, 245439 (2011).

[24] F. Leroy, F. Cheynis, T. Passanante, and P. Müller, Phys. Rev. B **85**, 195414 (2012).

[25] G. Boussinot and E. A. Brener, Phys. Rev. E **92**, 032408 (2015).

[26] J. Ye and C. V. Thompson, Phys. Rev. B **82**, 193408 (2010).

[27] J. Ye and C. V. Thompson, Adv. Mater. **23**, 1567 (2011).

[28] M. Abbarchi, M. Naffouti, M. Lodari, M. Salvalaglio, R. Backofen, T. Bottein, A. Voigt, T. David, J.-B. Claude, M. Bouabdellaoui *et al.*, Microelectron. Eng. **190**, 1 (2018).

[29] J. W. Cahn and J. E. Taylor, Acta Metall. Mater. **42**, 1045 (1994).

[30] W. Carter, A. Roosen, J. Cahn, and J. Taylor, Acta Metall. Mater. **43**, 4309 (1995).

[31] This regime actually accounts for both *attachment* and *detachment* process of material from the solid phase and it could be named including both these terms. However, following the nomenclature introduced in Ref. [30], we just refer to the entire process as SALK.

[32] W. W. Mullins, J. Appl. Phys. **27**, 900 (1956).

[33] W. W. Mullins, J. Appl. Phys. **28**, 333 (1957).

[34] See Supplemental Material at http://link.aps.org/supplemental/10.1103/PhysRevMaterials.3.103402 for more information on the experimental methods, details on high resolution TEM and AFM characterization, and on the theoretical approach used for simulations.

[35] W. Jiang, W. Bao, C. V. Thompson, and D. J. Srolovitz, Acta Materialia **60**, 5578 (2012).

[36] Y. Wang, W. Jiang, W. Bao, and D. J. Srolovitz, Phys. Rev. B **91**, 045303 (2015).

[37] W. Bao, W. Jiang, Y. Wang, and Q. Zhao, J. Comput. Phys. **330**, 380 (2017).

[38] W. Jiang and Q. Zhao, Phys. D (Amsterdam, Neth.) **390**, 69 (2019).

[39] E. Dornel, J. Barbé, J. Eymery, and F. de Crécy, MRS Proc. **910**, 0910-A04-05 (2006).

[40] D. T. Danielson, Anisotropic dewetting in ultra-thin single-crystal silicon-on-insulator films, Ph.D. thesis, Massachusetts Institute of Technology, Cambridge, MA, 2008.

[41] F. Cheynis, F. Leroy, and P. Müller, C. R. Phys. **14**, 578 (2013).

[42] S. Curiotto, F. Leroy, F. Cheynis, and P. Müller, Appl. Phys. Lett. **104**, 061603 (2014).

[43] V. Giliberti, E. Sakat, M. Bollani, M. V. Altoe, M. Melli, A. Weber-Bargioni, L. Baldassarre, M. Celebrano, J. Frigerio, G. Isella *et al.*, Small Methods **1**, 1600033 (2017).

[44] H.-C. Liu, Y.-H. Lin, and W. Hsu, Microsyst. Technol. **10**, 29 (2003).

[45] M. Aouassa, L. Favre, A. Ronda, H. Maaref, and I. Berbezier, New J. Phys. **14**, 063038 (2012).

[46] J. Rubinstein and P. Sternberg, IMA J. Appl. Math. **48**, 249 (1992).

[47] B. Li, J. Lowengrub, A. Rätz, and A. Voigt, Commun. Comput. Phys. **6**, 433 (2009).

[48] R. Bergamaschini, M. Salvalaglio, R. Backofen, A. Voigt, and F. Montalenti, Adv. Phys.: X **1**, 331 (2016).

[49] M. Brassel and E. Bretin, Math. Methods Appl. Sci. **34**, 1157 (2011).

[50] D. Lee and J. Kim, Math. Comp. Sim. **119**, 35 (2016).

[51] A. Rätz, A. Ribalta, and A. Voigt, J. Comput. Phys. **214**, 187 (2006).

[52] S. Torabi, J. Lowengrub, A. Voigt, and S. Wise, Proc. R. Soc. London **465**, 1337 (2009).

[53] M. Salvalaglio, R. Backofen, R. Bergamaschini, F. Montalenti, and A. Voigt, Cryst. Growth Design **15**, 2787 (2015).

[54] M. Salvalaglio, R. Backofen, A. Voigt, and F. Montalenti, Nanoscale Res. Lett. **12**, 554 (2017).

[55] M. Albani, L. Ghisalberti, R. Bergamaschini, M. Friedl, M. Salvalaglio, A. Voigt, F. Montalenti, G. Tütüncüoglu, A. Fontcuberta i Morral, and L. Miglio, Phys. Rev. Mat. **2**, 093404 (2018).

[56] M. Salvalaglio, P. Zaumseil, Y. Yamamoto, O. Skibitzki, R. Bergamaschini, T. Schroeder, A. Voigt, and G. Capellini, Appl. Phys. Lett. **112**, 022101 (2018).

[57] S. Vey and A. Voigt, Comput. Visual. Sci. **10**, 57 (2007).

[58] T. Witkowski, S. Ling, S. Praetorius, and A. Voigt, Adv. Comput. Math. **41**, 1145 (2015).

[59] R. Backofen, S. M. Wise, M. Salvalaglio, and A. Voigt, Int. J. Numer. Anal. Model. **16**, 192 (2019).

[60] P. Jacquet, R. Podor, J. Ravaux, J. Teisseire, I. Gozhyk, J. Jupille, and R. Lazzari, Scrip. Mater. **115**, 128 (2016).

[61] O. Kovalenko, J. Greer, and E. Rabkin, Acta Mater. **61**, 3148 (2013).

[62] S. W. Hieke, G. Dehm, and C. Scheu, Acta Mater. **140**, 355 (2017).

[63] Y. Ishikawa, M. Kumezawa, R. Nuryadi, and M. Tabe, Appl. Surf. Sci. **190**, 11 (2002).

[64] Y. Ishikawa, Y. Imai, H. Ikeda, and M. Tabe, Appl. Phys. Lett. **83**, 3162 (2003).

[65] F. Hackl, M. Grydlik, M. Brehm, H. Groiss, F. Schäffler, T. Fromherz, and G. Bauer, Nanotechnology **22**, 165302 (2011).

[66] E. Sakat, V. Giliberti, M. Bollani, A. Notargiacomo, M. Pea, M. Finazzi, G. Pellegrini, J.-P. Hugonin, A. Weber-Bargioni, M. Melli *et al.*, Phys. Rev. Appl. **8**, 054042 (2017).

[67] A. Branny, S. Kumar, R. Proux, and B. D. Gerardot, Nat. Commun. **8**, 15053 (2017).

[68] L. Kondic, J. A. Diez, P. D. Rack, Y. Guan, and J. D. Fowlkes, Phys. Rev. E **79**, 026302 (2009).

[69] G. H. Kim and C. V. Thompson, Acta Mater. **84**, 190 (2015).

[70] M. Kästner and B. Voigtländer, Phys. Rev. Lett. **82**, 2745 (1999).

[71] M. Brehm, H. Lichtenberger, T. Fromherz, and G. Springholz, Nanoscale Res. Lett. **6**, 70 (2011).

[72] J. J. Zhang, G. Katsaros, F. Montalenti, D. Scopece, R. O. Rezaev, C. Mickel, B. Rellinghaus, L. Miglio, S. DeFranceschi, A. Rastelli, and O. G. Schmidt, Phys. Rev. Lett. **109**, 085502 (2012).